Mid-Infrared Superchiral Field Induced by Quasi-Guided Mode in Diamond Metasurface

Hao Wang(王浩)[1,2], Shu Chen(陈述)[1], Xing Liu(刘星)[1], Yanan Yu(于亚楠)[1], Ziyi Lv(吕子怡)[1], Shengxiang Shan(单圣祥)[1], Tinghui Xiao(肖廷辉)[1,2,3,4*], and Chongxin Shan(单崇新)[1,2*]

[1]*Laboratory of Zhongyuan Light, School of Physics, Zhengzhou University, Zhengzhou 450001, China*
[2]*Henan Key Laboratory of Diamond Materials and Devices, Key Laboratory of Material Physics, Ministry of Education, School of Physics, Zhengzhou University, Zhengzhou 450052, China*
[3]*Institute of Quantum Materials and Physics, Henan Academy of Sciences, Zhengzhou 450046, China*
[4]*Department of Chemistry, School of Science, The University of Tokyo, Tokyo 113-0033, Japan*

(Received 15 August 2025; accepted manuscript online 23 October 2025)

The superchiral field that enables ultrasensitive detection and discrimination of chiral matter beyond that of circularly polarized light by its field structure has emerged as a powerful tool in chiroptical spectroscopy, spin photonics, and analytical chemistry. Specially, the superchiral field at the wavelength beyond 15 μm is indispensable for various mid-infrared applications, such as ultrasensitive chiroptical sensing in the molecular fingerprint region. Here we propose and present a new strategy to realize the superchiral field with a Kuhn's dissymmetric factor up to ∼90 at the wavelength beyond 15 μm. This is enabled by the high-quality (up to $\sim 10^4$) multipole resonance induced by Brillouin-zone-folding-driven quasi-guided mode in a diamond metasurface. This work opens up a new avenue towards realizing mid-infrared superchiral fields at the wavelength beyond 15 μm.

DOI: 10.1088/0256-307X/42/12/120405 CSTR: 32039.14.0256-307X.42.12.120405

1. Introduction. Superchiral fields are optical fields whose structural chirality exceeds that of circularly polarized light (CPL), thereby resulting in significantly stronger chiral dissymmetry in specific spatial regions. This structural chirality is quantified by the Kuhn's dissymmetric factor, which represents the optical chirality normalized to the optical intensity.[1–3] The superchiral field that enables ultrasensitive detection and discrimination of chiral matter beyond that of CPL by its field structure has emerged as a new powerful tool in chiroptical spectroscopy, spin photonics, and analytical chemistry.[4–7] It is far more efficient than CPL to probe or interact with chiral matter, from chiral molecules to chiral nanomaterials.[8,9] For instance, the superchiral field has been utilized to achieve remarkable enantioselectivity in the optical excitation of chiral molecules.[10] Recently, it has also been employed to amplify the chiral-to-achiral signal ratio in circular dichroism.[11,12] These exceptional attributes make the superchiral field highly sought after for achieving extraordinarily strong chiral light-matter interactions, unlocking various applications such as ultrasensitive detection of chiral molecules, enantioselective optical manipulation, and efficient generation of chiral photons.[13–15]

Recently, a range of innovative strategies has been proposed to generate superchiral electromagnetic fields, significantly advancing the field of chiral light-matter interactions. One prominent approach relies on interference-based methods, in which multiple beams of circularly or elliptically polarized light are superimposed in free space to produce superchiral fields.[1,16] Nevertheless, these superchiral fields typically emerge in regions of destructive interference, inherently reducing the overall optical field intensity. An alternative and widely explored method employs plasmonic nanostructures. By engineering metallic nanostructures to support localized surface plasmon resonances, highly confined and intense superchiral fields can be achieved.[17,18] Unfortunately, the predominantly linear polarization characteristic of plasmonic resonances presents a major obstacle in producing single-sign superchiral fields—those that are uniformly positive or negative—throughout the near-field region. This limitation compromises the consistency and reproducibility of chiral light-matter interactions at nanoscale.[19] Dielectric nanoresonators have also been investigated as platforms for superchiral field generation via engineered Mie resonances.[20–23] These structures offer greater polarization flexibility, as they can support a broad range of resonant modes with diverse polarization symmetries, and are thus less constrained by linear polarization.[3,24] Meanwhile, several advanced photonic design strategies, including Brillouin-zone folding and guided-mode resonance, have recently been developed to enable strong optical confinement and achieve high-Q resonances.[25–29] These approaches offer a promising and complementary routine towards enhancing light-matter interactions. Nonetheless, their potential for the generation of superchiral electromagnetic fields remains largely unexplored, particularly in the spectral range beyond 15 μm, which is essential

*Corresponding authors. Email: xiaoth@zzu.edu.cn; cxshan@zzu.edu.cn
© 2025 Chinese Physical Society and IOP Publishing Ltd. All rights, including for text and data mining, AI training, and similar technologies, are reserved.

for diverse mid-infrared applications, such as ultrasensitive chiroptical sensing within the molecular fingerprint region.[30,31]

In this work, we propose and theoretically present the superchiral field with a Kuhn's dissymmetric factor up to ∼90 at the wavelength beyond 15 µm. This is enabled by the high-quality multipole resonance in diamond tetramers induced by Brillouin zone folding driven quasi-guided mode in a diamond metasurface. Two induced quasi-guided modes with different multipole resonances are systematically investigated for achieving superchiral fields as a function of the asymmetric parameter. Due to the different polarization symmetries of the excited multipole resonances, the two induced quasi-guided modes exhibit completely different optical chirality and dissymmetric factors. This work opens up a new avenue towards mid-infrared superchiral fields at the wavelength beyond 15 µm.

2. Results and Discussion. The concept of mid-infrared superchiral field induced by Brillouin zone folding driven quasi-guided mode in a diamond metasurface with C_4 symmetry properties is proposed and schematically illustrated in Fig. 1(a). As the incident light used to interact with our structure is CPL which is chiral, the generated optical near-field within our structure is chiral. The diamond metasurface is designed as a periodic array of tetramers arranged in a square lattice, with each tetramer consisting of four identical microcubes [see Sections 1 and 2 in Supplementary Materials (SM) for details]. The upper panel of Fig. 1(b) illustrates the specific geometric parameters of the diamond metasurface in its initial state that supports guided modes, featuring a unit cell period $p_0 = 7.2\,\mu\text{m}$, a microcube width $w = 4.4\,\mu\text{m}$, a microcube height $h = 3.1\,\mu\text{m}$, and a gap distance $s = p_0 - w = 2.8\,\mu\text{m}$. Regarding the chosen height of 3.1 µm, it was selected to ensure vertical optical confinement while staying within the reported etching depth limit for diamond (see Section 3 in SM for details).[32] As guided modes are non-radiative, it is essential to convert guided modes into quasi-guided modes for far-field excitation. This is achieved by in-plane translational symmetry breaking via simultaneously moving four adjacent microcubes toward their center to form a tetramer. The gap distance in the tetramer is denoted as s' shown in the lower panel of Fig. 1(b). With this movement, the period of the metasurface is doubled, resulting in the Brillouin zone folding and the emergence of quasi-guided modes.[33,34] With the normal incidence of mid-infrared CPL, the quasi-guided modes are excited within the diamond metasurface, which leads to the mid-infrared superchiral field in the near-field region. The Brillouin zone folding induced by periodic perturbations can lead to both quasi-guided mode and bound-states in the continuum (BIC), which can be distinguished by their Q-factor behaviors in the momentum space. The Q factor of quasi-guided mode shows a flat feature in the momentum

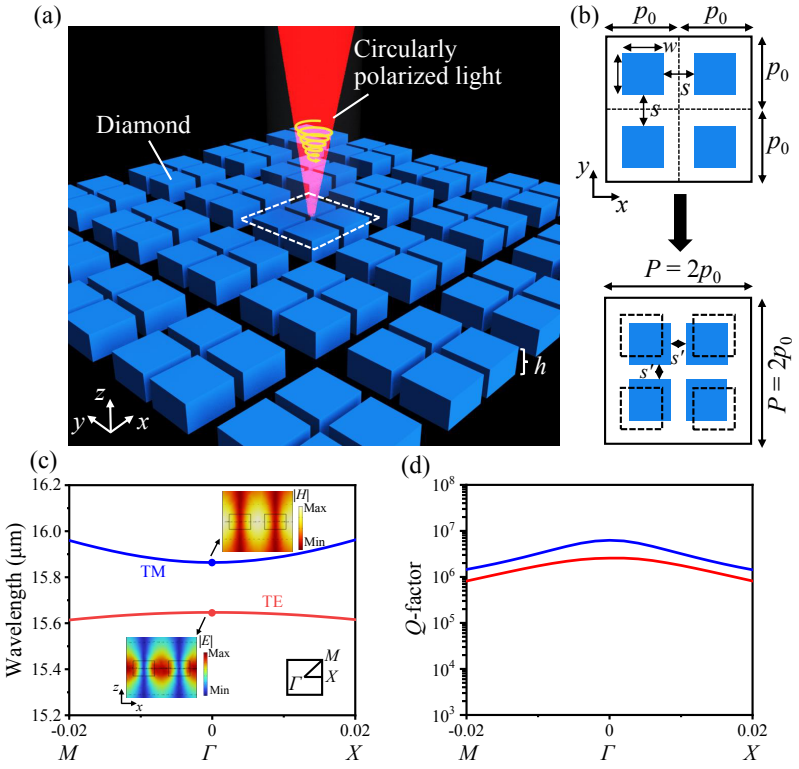

Fig. 1. Concept of mid-infrared superchiral field induced by Brillouin zone folding driven quasi-guided mode in the diamond metasurface. (a) The diamond metasurface is composed of microcube tetramers with a height $h = 3.1\,\mu\text{m}$. (b) The upper panel shows the initial state of four adjacent diamond microcubes before clustering into tetramers, with its geometric parameters: $p_0 = 7.2\,\mu\text{m}$, $w = 4.4\,\mu\text{m}$, $h = 3.1\,\mu\text{m}$, and $s = 2.8\,\mu\text{m}$. The lower panel shows the diamond tetramers formed after the movement. The period P is changed to $2p_0$ and the gap distance s altered to s'. (c) Photonic bands that correspond to the two resonant modes. The insets show the corresponding electric and magnetic field distributions at the Γ point. (d) Q factors of the two resonant modes in the momentum space.

space while the Q factor of BIC shows a sharp feature.[35] Based on this, we calculated the photonic bands and Q factors of the two resonant modes in the momentum space, as shown in Figs. 1(c) and 1(d). Two eigenmodes with wavelengths exceeding 15 μm were selected as the resonant modes. The lower branch (red curve) corresponds to a TE mode while the upper branch (blue curve) corresponds to a TM mode, which are verified by their electric and magnetic field distributions as shown in the insets. To gain insight into their radiation characteristics, we analyzed the Q factors of these modes in the momentum space. It is clear that the Q factors of the two resonant modes exhibit flat features in the momentum space, indicating that the two resonant modes are quasi-guided modes.

Based on the above concept and design, we first study the mid-infrared optical response of the proposed diamond metasurface. The perturbation before and after the movement of diamond microcubes is quantified by an asymmetry parameter $\alpha = (s - s')/s$. The transmission spectra of the diamond metasurface with different values of the asymmetry parameter α are calculated and shown in Fig. 2(a). With $\alpha = 0$, no transmission valleys are observable, which is due to the non-radiative character of guided modes supported by the symmetric structure of the diamond metasurface. As the value of the asymmetry parameter α increases, the in-plane translational symmetry of the diamond metasuface is broken, leading to the Brillouin zone folding and the emergence of two quasi-guided modes with Fano line shapes (see Section 4 in SM for details). The relations between the asymmetry parameter α and the quality Q factors of these two quasi-guided modes are investigated and shown in Figs. 2(b) and 2(c). As the asymmetry parameter α increases, the Q factor gradually decreases, which follows an inverse quadratic law (i.e., $Q \propto \alpha^{-2}$) by a curve fitting. This agrees well with the feature of guided modes.[26] The Q factor of Mode 2 is about one order of magnitude larger than that of Mode 1 (see Section 5 in SM for details). To elucidate the physical origin of the

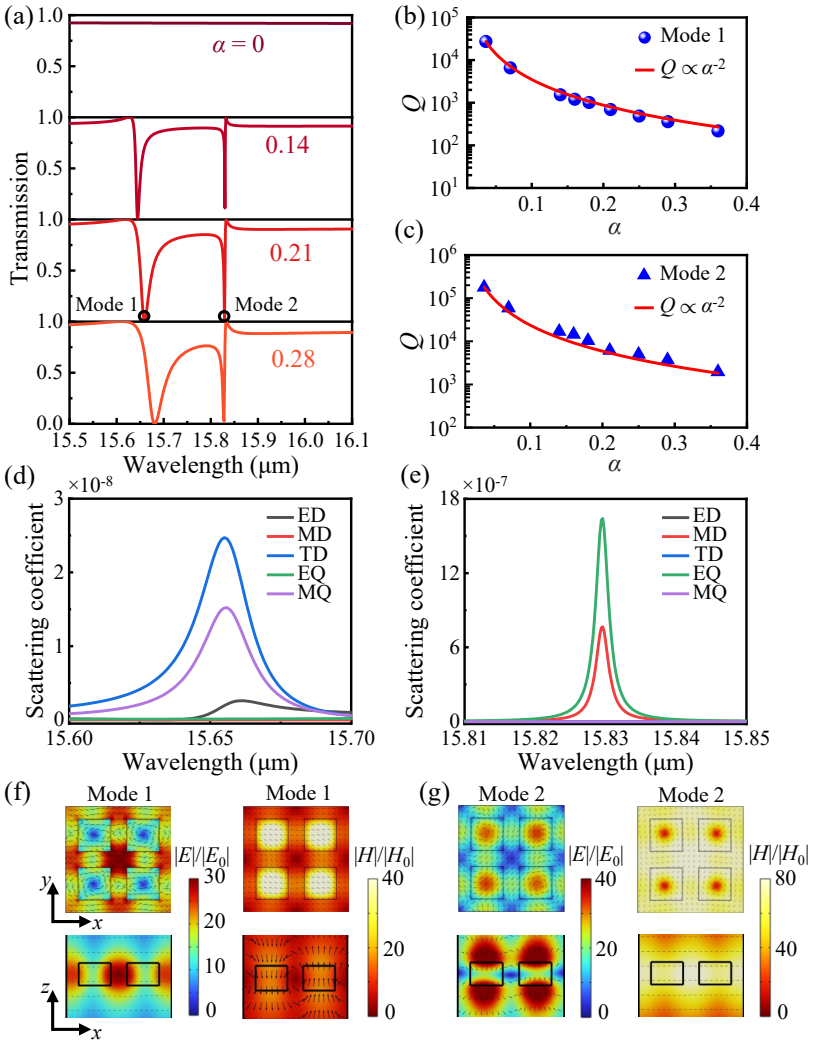

Fig. 2. Optical response of the proposed diamond metasurface and multipole expansion analysis of two quasi-guided modes with an asymmetric factor α. (a) Transmission spectrum of the proposed mid-infrared diamond metasurface with a varying asymmetric factor α. Q factors of (b) Mode 1 and (c) Mode 2 as a function of the asymmetric parameter α. Multipole expansion of the scattering spectra of the diamond metasurface with (d) Mode 1 and (e) Mode 2 ($\alpha = 0.21$). Top and side views of the normalized electric-field and magnetic-field magnitude distributions corresponding to (f) Mode 1 and (g) Mode 2, showing the xy plane ($z = h/2 = 1.55$ μm) and the zx plane ($y = 0$ μm) with an asymmetric factor $\alpha = 0.21$.

two excited quasi-guided modes, the multipole expansion analysis is used for the diamond metasurface with $\alpha = 0.21$ as shown in Figs. 2(d) and 2(e) (see Section 6 in SM for details). Mode 1 is primarily contributed by the combination of toroidal dipole (TD), magnetic quadrupole (MQ), and electric dipole (ED) while Mode 2 is mainly contributed by the combination of electric quadrupole (EQ) and magnetic dipole (MD). The distinct compositions result in the completely different electric-field and magnetic-field distributions of the two quasi-guided modes shown in Figs. 2(f) and 2(g), respectively. For Mode 1, the electric field is primarily concentrated in the air gap region of each tetramer, which corresponds to an air mode. In contrast, for Mode 2, the electric field is primarily concentrated in the microcubes, which corresponds to a dielectric mode. This results in their different resonant-wavelength sensitivities to the asymmetry parameter α shown in Fig. 2(a). In addition, Mode 2 exhibits a stronger electromagnetic field than that of Mode 1, which agrees with its higher Q factor (up to $\sim 10^4$). This is also verified by their volume-averaged electromagnetic enhancement factors (see Section 7 in SM for details).

With these two mid-infrared quasi-guided modes, we further investigate their near-field optical chirality with the incidence of right CPL as a representative case. Notably, since the diamond metasurface is achiral, the optical chirality excited with the incidence of left CPL is identical but with an opposite sign (see Section 8 in SM for details). To demonstrate the practical utility of the two quasi-guided modes for studying enhanced chiral light-matter interactions, we calculate the normalized volume-averaged optical chirality $C_{\text{E_ave}}$ in the near-field air region of the metasurface. $C_{\text{E_ave}}$ is defined as

$$C_{\text{E_ave}} = \frac{\int C_{\text{E}}(x,y,z)\mathrm{d}v}{\int \mathrm{d}v} = \frac{\int C(x,y,z)/|C_{\text{CPL}}|\mathrm{d}v}{\int \mathrm{d}v}, \quad (1)$$

where $C_{\text{E}}(x,y,z) = C(x,y,z)/|C_{\text{CPL}}|$ is the normalized optical chirality, $C(x,y,z) = -\frac{\omega}{2c^2}\text{Im}[\boldsymbol{E}^*(x,y,z)\cdot \boldsymbol{H}(x,y,z)]$ is the optical chirality. $C_{\text{CPL}} = \pm\frac{\varepsilon_0\omega}{2c}E_0^2$ is the optical chirality of free-space CPL, where c and ω represent the speed and the angular frequency of light, ε_0 is the permittivity of air, $\boldsymbol{E}(x,y,z)$ is the electric field, $\boldsymbol{H}(x,y,z)$ is the magnetic field, E_0 represents the electric field magnitude of the incident CPL, and v is the volume of the near-field air region. With the normal incidence of right CPL, the normalized volume-averaged optical chirality $C_{\text{E_ave}}$ as a function of the incident wavelength for different values of the asymmetric factor α is shown in Fig. 3(a) (see Sections 9 and 10 in SM for details). With $\alpha = 0$, the normalized optical chirality remains almost a constant with a value of one in the mid-infrared wavelength range from 15.5 to 16.1 μm. This indicates that the optical chirality induced by the guided modes are not observable, which is due to their non-radiative property that prevents far-field excitation. By breaking the in-plane translational symmetry of the diamond metasurface, two distinct peaks with Fano lineshapes are observed at the wavelengths that correspond to two quasi-guided modes. Interestingly, the two quasi-guided modes exhibit completely different values of the normalized volume-averaged optical chirality. The normalized volume-averaged optical chirality of Mode 1 is minuscule (down to ~ 1 with the asymmetric factor $\alpha = 0.28$) and decreases gradually with the increase of the asymmetric factor α. Its minuscule volume-average value arises from the coexistence of both positive and negative optical chirality in the near-field region as shown in the upper panels of Fig. 3(b). As Mode 1 is an air mode, its optical field becomes more linearly polarized with the narrowing of the air gaps. This leads to the decrease of optical chirality with the increase of the asymmetric factor α, which is verified by the variation of the optical chirality distributions shown in the upper panels of Fig. 3(b). In

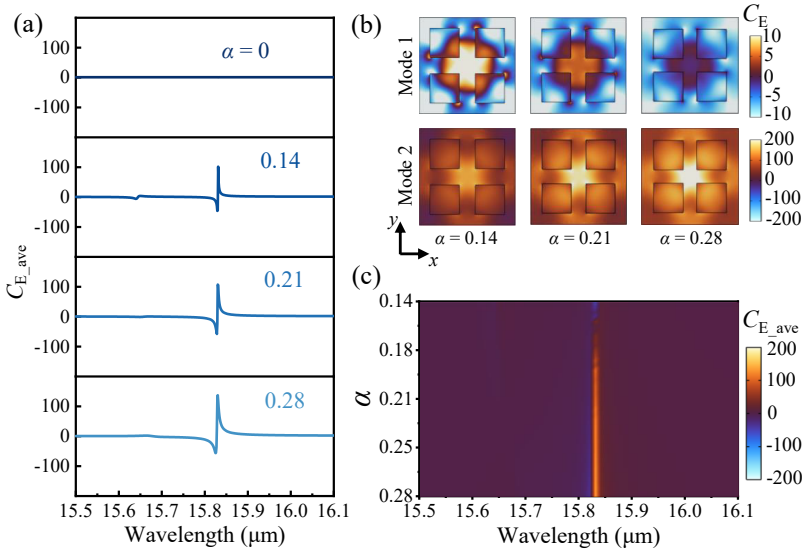

Fig. 3. Optical chirality analysis of the proposed diamond metasurface. (a) Normalized volume-averaged optical chirality $C_{\text{E_ave}}$ as a function of the incident wavelength for different values of the asymmetric factor α. (b) Top views of the normalized optical chirality C_{E} of the two quasi-guided modes with the asymmetric factor $\alpha = 0.14$, 0.21, and 0.28, respectively. (c) Spectrum of the normalized volume-averaged optical chirality $C_{\text{E_ave}}$, tuned by the asymmetric factor α.

contrast, the normalized volume-averaged optical chirality of Mode 2 is giant (up to ∼137 with the asymmetric factor $\alpha = 0.28$) and increases gradually with the increase of the asymmetric factor α. Its giant volume-average value results from the single-sign optical chirality distribution in the near-field region as shown in the lower panels of Fig. 3(b). As Mode 2 is a dielectric mode, its optical field is less prone to linear polarization effects and instead becomes more confined and intensified with reduced air gaps (see Section 11 in SM for details). Its optical chirality is thus increased with the increase of the asymmetric factor α, which is verified by the variation of the optical chirality distributions shown in the lower panels of Fig. 3(b). Moreover, the spectrum of the normalized volume-averaged optical chirality $C_{\mathrm{E_ave}}$, with a varying asymmetric factor α is calculated and shown in Fig. 3(c), which indicates the inducibility and tunability of mid-infrared optical chirality by Brillouin zone folding and asymmetry tuning, respectively.

Based on the above analysis and tunability of mid-infrared optical chirality, we study the mid-infrared superchiral field induced by Brillouin zone folding of guided modes in the diamond metasurface. The Kuhn's dissymmetry factor, which is defined as

$$g_{\mathrm{E}}(x, y, z) = 2cC(x, y, z)/\varepsilon_0\omega|E(x, y, z)|^2, \qquad (2)$$

is introduced to quantify the superchiral field normalized to that of CPL. The dissymmetry factor is a physical quantity that describes the structural chirality of the optical field. Specifically, it represents the optical chirality normalized to the optical intensity. This factor reflects the local enhancement of chiral light–matter interaction relative to total light–matter interaction. The maximum Kuhn's dissymmetry factor $g_{\mathrm{E_max}}$ as a function of the incident wavelength for different values of the asymmetric factor α is shown in Fig. 4(a) (see Section 12 in SM for details). The evaluation volume for $g_{\mathrm{E_max}}$ was chosen as the air gap region at the center of the diamond tetramers. With $\alpha = 0$, the $g_{\mathrm{E_max}}$ remains close to zero, indicating the absence of superchiral field, which is consistent with that of optical chirality. This is also due to the non-radiative property of the guided modes that prevents the far-field excitation. By increasing the asymmetric factor α to break the translational symmetry of guided modes, a Kuhn's dissymmetry factor peak emerges at the wavelength that correspond to Mode 2, signifying the generation of mid-infrared superchiral field within the diamond metasurface. Moreover, with the increase of the asymmetric factor α, the Kuhn's dissymmetric factor is also gradually increased. In contrast, there is not an evident peak at the wavelength that correspond to Mode 1. This agrees well with that of optical chirality since the Kuhn's dissymmetric factor is proportional to optical chirality as indicated by Eq. (2). To further elucidate the spatial characteristics of the induced superchiral fields, we compute the spatial distribution of $g_{\mathrm{E_max}}$ for different asymmetry factors at the resonant wavelengths of the two quasi-guided modes, as illustrated in Fig. 4(b). The superchiral field for Mode 1 is with a minuscule Kuhn's dissymmetry factor and mainly concentrated in the centers of the diamond microcubes while the superchiral field for Mode 2 is with a maximum Kuhn's dissymmetry factor up to ∼45 and mainly concentrated in the air gap center of the diamond tetramers. It is also verified from Fig. 4(b) that the Kuhn's dissymmetric factor of the superchiral field is increased with the increase of the asymmetric factor. Additionally, the resonant wavelength of the superchiral field associated with quasi-guided modes can be tuned by adjusting the width of the diamond microcubes, as shown in Fig. 4(c). As microcube width w increases, the resonance corresponding to Mode 2 undergoes a redshift, consistent with its dielectric mode nature. The superchiral field demonstrates reduced

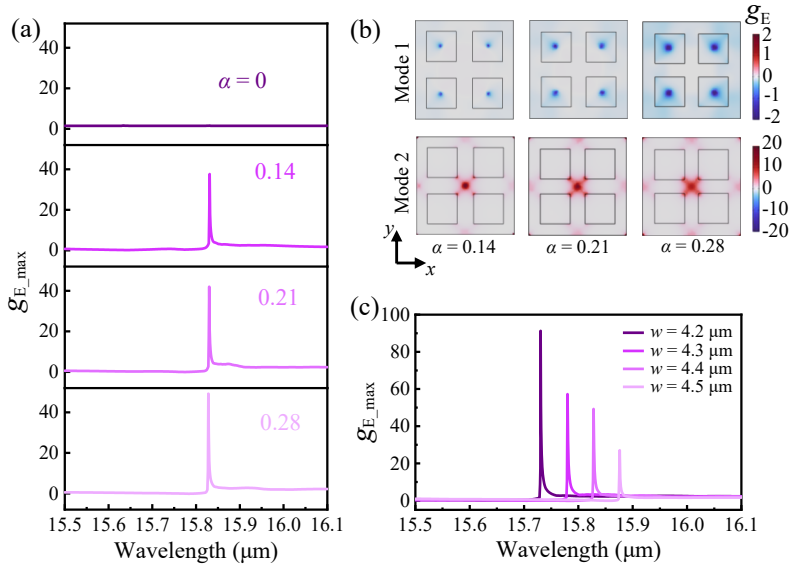

Fig. 4. Kuhn's dissymmetric factor analysis of the proposed diamond metasurface. (a) Normalized maximum dissymmetry factor $g_{\mathrm{E_max}}$ as a function of the incident wavelength for different values of the asymmetric factor α. (b) Top views of the normalized dissymmetry factor g_{E} of the two quasi-guided modes with the asymmetric factor $\alpha = 0.14$, 0.21, and 0.28, respectively. (c) Normalized maximum dissymmetry factor $g_{\mathrm{E_max}}$ as a function of the incident wavelength for different values of the microcube width w.

susceptibility to linear polarization effects while exhibiting enhanced field confinement and intensity at smaller air area.

3. Conclusion. In summary, we propose and present mid-infrared superchiral field at the wavelength beyond 15 μm. This is enabled by the high-Q (up to $\sim 10^4$) multipole resonance in diamond tetramers induced by Brillouin-zone-folding-driven quasi-guided mode in a diamond metasurface. Specifically, the in-plane translational symmetry of the diamond metasuface is broken by perturbing its period, leading to the Brillouin zone folding and the transition from ideal guided to quasi-guided modes. The different polarization symmetries of the two quasi-guided modes that correspond to air and dielectric modes result in fundamentally different optical chirality and dissymmetry factors. Notably, the quasi-guided mode corresponding to the dielectric mode of the diamond tetramer demonstrates superior performance, generating mid-infrared superchiral fields with a volume-averaged optical chirality up to ∼137 and a Kuhn's dissymmetry factor reaching ∼90. This work not only provides a new physical mechanism but also a new integrated photonic platform for achieving mid-infrared superchiral fields at the wavelength beyond 15 μm. It holds considerable potential for practical applications in chiroptical spectroscopy, spin photonics, and analytical chemistry.

Acknowledgements. This work was supported by the National Key R&D Program of China (Grant No. 2024YFE0105200) and the National Nature Science Foundation of China (Grant No. 62405284).

References

[1] Tang Y and Cohen A E 2010 *Phys. Rev. Lett.* **104** 163901
[2] Hendry E, Carpy T, Johnston J, Popland M, Mikhaylovskiy R V, Lapthorn A J, Kelly S M, Barron L D, Gadegaard N, and Kadodwala M 2010 *Nat. Nanotechnol.* **5** 783
[3] Xiao T H, Cheng Z, Luo Z, Isozaki A, Hiramatsu K, Itoh T, Nomura M, Iwamoto S, and Goda K 2021 *Nat. Commun.* **12** 3062
[4] Kakkar T, Keijzer C, Rodier M, Bukharova T, Taliansky M, Love A J, Milner J J, Karimullah A S, Barron L D, Gadegaard N, Lapthorn A J, and Kadodwala M 2020 *Light: Sci. Appl.* **9** 195
[5] Tan Y, Lu X and Ding T 2024 *ACS Sens.* **9** 3290
[6] Cheng C C, Cheng P J, Huang T W, Wang W T, Tsai J T, Shih M H, and Chang S W 2023 *Optica* **10** 732
[7] Yamane H, Yokoshi N, Ishihara H, and Oka H 2023 *Opt. Express* **31** 13708
[8] Hu L, Sun Z, Nie Y, Huang Y, and Fang Y 2022 *Laser Photonics Rev.* **16** 2200035
[9] Barkaoui H, Du K, Chen Y, Xiao S, and Song Q 2023 *Phys. Rev. B* **107** 045305
[10] Tang Y and Cohen A E 2011 *Science* **332** 333
[11] Biswas A, Cencillo-Abad P, Shabbir M W, Karmakar M, and Chanda D 2024 *Sci. Adv.* **10** eadk2560
[12] Xu C, Ren Z, Zhou H, Zhou J, Ho C P, Wang N, and Lee C 2023 *Light: Sci. Appl.* **12** 154
[13] Lininger A, Palermo G, Guglielmelli A, Nicoletta G, Goel M, Hinczewski M, and Strangi G 2023 *Adv. Mater.* **35** 2107325
[14] Wu T, Hou S, Zhang W, and Zhang X 2020 *Phys. Rev. A* **102** 053519
[15] Gou Y, Ma H F, Wang Z X, Wu L W, Wu R Y, and Cui T J 2022 *Opt. Express* **30** 12775
[16] Kang L, Ren Q, and Werner D H 2017 *ACS Photonics* **4** 1298
[17] Vázquez-Guardado A and Chanda D 2018 *Phys. Rev. Lett.* **120** 137601
[18] Tabouillot V, Kumar R, Lalaguna P L, Hajji M, Clarke R, Karimullah A S, Thomson A R, Sutherland A, Gadegaard N, Hashiyada S, and Kadodwala M 2022 *ACS Photonics* **9** 3617
[19] Schäferling M, Dregely D, Hentschel M, and Giessen H 2012 *Phys. Rev. X* **2** 031010
[20] Xiao T, Cheng Z, and Goda K 2018 *Small* **14** 1800485
[21] Pura J L, Castillo López De Larrinzar B, Liang M, García-Martín A, Gómez Rivas J, and Sánchez-Gil J A 2024 *ACS Photonics* **11** 4090
[22] Sun Y, He C, Deng Z, Li X, Li X, Zhang Z, Sui X, Li N, He W, and Chen F 2025 *Nanophotonics* **14** 559
[23] Wang H, Chen S, Liu X, Yu Y, Xiao T H, and Shan C X 2025 *Opt. Lett.* **50** 1381
[24] Kuznetsov A I, Miroshnichenko A E, Brongersma M L, Kivshar Y S, and Luk'yanchuk B 2016 *Science* **354** aag2472
[25] Yan X, Xie Y, Chen S, and Wu P 2024 *Adv. Opt. Mater.* **12** 2401027
[26] Mo H C, Zhang W J, Wu Z Y, Chen X D, and Dong J 2025 *ACS Photonics* **12** 2795
[27] Zhang Y, Wang L, Wang Y, He H, Duan H, Gao C, You S, Qiu M, and Zhou C 2024 *Appl. Phys. Lett.* **125** 241701
[28] Li J, Duan Q, Dong X, Yang Z, Hu Y, Zhi J, Zhu S, and Chen H 2025 *Appl. Phys. Lett.* **126** 241702
[29] Yue L, Xie P, Ding Q, Zhou X, Shen S, and Wang W 2025 *Phys. Rev. B* **111** 045412
[30] Xiao T H, Zhao Z, Zhou W, Takenaka M, Tsang H K, Cheng Z, and Goda K 2017 *Opt. Lett.* **42** 2882
[31] Li Y, Chen S, Yu Y, Li C, and Xiao T 2024 *Opt. Lett.* **49** 3620
[32] Toros A, Kiss M, Graziosi T, Mi S, Berrazouane R, Naamoun M, Vukajlovic Plestina J, Gallo P, and Quack N 2020 *Diam. Relat. Mater.* **108** 107839
[33] Sun K, Wei H, Chen W, Chen Y, Cai Y, Qiu C W, and Han Z 2023 *Phys. Rev. B* **107** 115415
[34] Sun K, Wang W, and Han Z 2024 *Phys. Rev. B* **109** 085426
[35] Wang W, Srivastava Y K, Tan T C, Wang Z, and Singh R 2023 *Nat. Commun.* **14** 2811